Chinese Journal of Aeronautics 25 (2012) 524-532

Contents lists available at ScienceDirect

Chinese Journal of Aeronautics

journal homepage: www.elsevier.com/locate/cja

Flow and Heat Transfer Characteristics in Rotating Two-pass Channels Cooled by Superheated Steam

WANG Wei, GAO Jianmin, XU Liang*, SHI Xiaojun

State Key Laboratory for Manufacturing Systems Engineering, Xi'an Jiaotong University, Xi'an 710049, China

Received 7 June 2011; revised 26 July 2011; accepted 1 November 2011

Abstract

In a modern gas turbine, using superheated steam to cool the vane and blade for internal convection cooling is a promising alternative to traditional compressor air. However, further investigations of steam cooling need to be performed. In this paper, the three-dimensional flow and heat transfer characteristics of steam are numerically investigated in two-pass square channels with 45° ribbed walls under stationary and rotating conditions. The investigated rotation numbers are 0 and 0.24. The simulation is carried out by solving the Reynolds averaged Navier-Stokes equations employing the Reynolds stress turbulence model, especially considering two additional terms for Coriolis and rotational buoyancy forces caused by the rotating effect. For comparison, calculations for the air-cooled channels are done first at a Reynolds number of 25 000 and inlet coolant-to-wall density ratio of 0.13. The results are compared with the experiment data. Then the flow and heat transfer in steam-cooled channels are analyzed under the same operating conditions. The results indicate that the superheated steam has better heat transfer performance than air. Due to the combined effect of rotation, skewed ribs and 180° sharp turn, the secondary flow pattern in steam-cooled rotating two-pass channels is quite complex. This complex secondary flow pattern leads to strong anisotropic turbulence and high level of anisotropy of Reynolds stresses, which have a significant impact on the local heat transfer coefficient distributions.

Keywords: turbine; steam cooling; rotation; numerical analysis; heat transfer; secondary flow; Reynolds stress

1. Introduction

Increasing the inlet gas temperature of blade channels in gas turbine is one of the most effective ways to enhance the overall thermal efficiency and output power. Nowadays turbine inlet temperature has reached 2 200 K, which far exceeds the allowable metal temperature of turbine blades. Thus, efficient cooling of the vanes and blades becomes necessary. Highly sophisticate cooling techniques have been employed for modern turbine blades, such as film cooling [1-2], pin-fin cooling [3-5], rib turbulated cooling [6-7], jet impingement cooling [8-9] and transpiration cooling [10]. For rib turbulated cooling, it is widely used as internal blade cooling in a serpentine flow path for the rotating blades. It has been demonstrated that rotation can significantly alter the local heat transfer in the internal coolant passages [11-12]. Therefore flow structure and local heat transfer characteristics in the U channels with ribs under the conditions of rotation are always the important research topics.

Wagner, et al. [11-14] experimentally analyzed the combined effect of Coriolis and rotating buoyancy forces on flow fields and local heat transfer distributions in rotating multipass internal coolant passage with smooth walls and normal ribs as well as skewed ribs. They showed that the Coriolis forces led to increased heat transfer on the trailing wall in the flow radial outward passage, while heat transfer on the leading wall was decreased. The opposite effect can be found for radial inward flow. The skewed ribs provided

*Corresponding author. Tel.: +86-29-83395089.
E-mail address: xuliang@mail.xjtu.edu.cn
Foundation items: National Basic Research Program of China (2007CB707701); National Natural Science Foundation of China (51106124); Research Fund for the Doctoral Program of Higher Education of China (20100201120007)

doi: 10.1016/S1000-9361(11)60416-0

higher heat transfer coefficients and less sensitivity to buoyancy effects and those skewed ribs, rather than normal ribs, should be employed for rotating coolant passages. Han and Zhang experimentally investigated the effect of wall heating condition on the local heat transfer coefficient in a rotating square channel with smooth walls and radial outward flow [15]. They also investigated the effects of ribs with different configurations [16-18] and channel orientation [19] on heat transfer in a two-pass rectangular rotating channel, as well as the effects of the entrance geometry [20].

In addition to the experimental studies mentioned above, many numerical studies of flow and heat transfer behavior have been performed. Dutta, et al. [21] used a two-equation k-ε turbulence model with new terms for Coriolis and rotational buoyancy to predict the heat transfer in a rotating square channel. Stephens, et al. [22] employed a low-Reynolds-number k-ω model of turbulence to predict the three-dimensional flow in a rotating two-passage square duct. The computed heat transfer coefficients on the leading surface in the first passage were overestimated. Chen, et al. [23-24] is the first to accurately predict the flow and heat transfer behavior in a rotating two-pass square duct with smooth walls by performing a near-wall second moment turbulence closure model. He demonstrated the superiority of the second-order Reynolds stress closure models over simpler k-ε isotropic eddy viscosity models, i.e., the second-moment solutions exhibit a significant level of anisotropy in the normal components of Reynolds stress tensor and is suitable for predicting the flow and heat transfer in rotating passages with strong nonisptropic produced by the Coriolis and centrifugal buoyancy forces. With the same second-moment closure model, Al-Qahtani, et al. [25] then predicted the flow and heat transfer in a rotating two-pass rectangular channel with 45° angled ribs. This complex three-dimensional flow and heat transfer characteristics resulting from rotation, angled ribs and sharp 180° turn can be predicted fairly well.

These above referenced papers are very informative, but unfortunately, they do not present an investigation of the effects of the coolant medium on the flow field and heat transfer. They all use compressor air as cooling fluid. While recently the alternative coolant such as water and steam are selected. And these cooling types can greatly save the air form the compressor. Especially, the process steam with favorable fluid properties can provide several benefits as cooling fluid, in comparison to air-cooling [26-28]. There are also some studies on gas turbines with steam cooling (Corman [29] and Fukue [30]). In the present study, the flow field and heat transfer of coolant air and steam are comparatively analyzed in the rotating two-pass square ducts with 45° angled ribs.

2. Numerical Methodologies

2.1. Geometry and grid generation

The present calculations are performed for a two-pass rectangular channel with 45° angled ribs, which is the same as the experimental configuration of Wagner, et al. [11]. Figure 1 shows the investigated geometry and grids. It has two-pass square channels connected by a sharp 180° turning. Both channels consist of unheated smooth section (L_1=10D_h) and heated ribbed section (L_2=14D_h). The channel hydraulic diameter D_h is 12.7 mm. The radius of turning r_1 is 1.25D_h and the distance between the rotating axis and the inlet R_r is 32D_h. Two opposite walls, which are denoted as the leading and trailing surfaces respectively, are roughed with 45° parallel ribs. These square-cross section ribs are equally spaced on the leading and trailing surfaces alternately. The rib height-to-hydraulic diameter ratio (e/D_h) is 0.1, and the rib pitch-to-height ratio (P/e) is 10. The distance between the inlet and the first rib on the trailing surface is 2.46D_h.

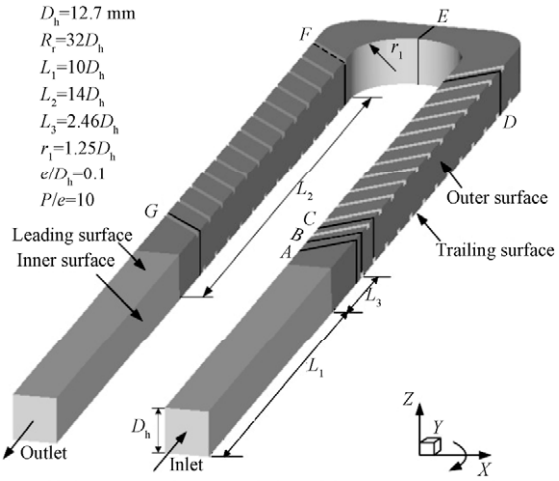

(a) Geometry and conceptual view of the two-pass rectangular channel with 45° angled ribs

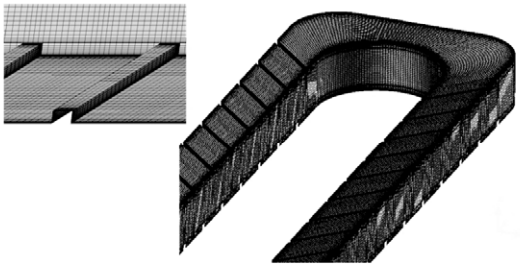

(b) Numerical grids for the two-pass rectangular channel with 45° angled ribs

Fig. 1 The investigated geometry and grids.

The block-structured hexahedral meshes are generated by ICEM CFD 11.0 software. To provide adequate resolutions of the viscous sublayer and buffer layer adjacent to a solid surface, the minimum grid spacing in the near-wall region is maintained at 10^{-4} of body length, which corresponds to a wall coordinate y^+ around 1 [31].

2.2. Computational code and turbulence model

The numerical solutions are performed by using commercial software ANSYS CFX 11.0, based on fi-

nite volume technique. The equations (the mass, momentum and energy) are discretized and solved iteratively for each control volume. As a result, an approximation of the value of each variable at specific points throughout the domain can be obtained [29]. A convergence criterion of 10^{-5} is used for the maximum root mean square (RMS) error in all computational blocks.

Because of the strong anisotropy of Reynolds stress in the calculated channels, the ω Reynolds stress model based on the ω-equation is selected as the turbulence model with automatic wall function. Though this model is developed originally for incompressible flows in non-rotating coordinates, it is now generalized to include the effects of rotation.

2.3 Boundary conditions

The experimental boundary conditions of Wagner, et al. [11] are adopted as reference. The coolant fluid at the entrance of the duct is at a uniform temperature of T_0, dimensionless temperature $\theta=(T-T_0)/(T_w-T_0)=0$, where T_w is the wall surface temperature, and T the local temperature. The temperature of all heated walls including ribs are fixed at $T=T_w$ ($\theta=1$). The type of wall boundary condition implementation is set to be no slip. The inlet coolant-to-wall density ratio ($\Delta\rho/\rho=(T_w-T_0)/T_w$) is 0.13. A static pressure of 1.0×10^6 Pa is imposed at the outlet. The investigated Reynolds number $Re=\rho W_b D_h/\mu$ is 25 000, and the rotation numbers $Ro=\Omega D_h/W_b$ are 0 and 0.24, where W_b is the bulk velocity in streamwise direction, μ the dynamic viscosity, and Ω the rotational speed.

In the calculations, the thermodynamic and transport properties of superheated steam are determined by calculating formulation called "IAPWS Industrial Formulation 1997 for the Thermodynamic Properties of Water and Steam (IAPWS-IF97 for short) [32]", which is an approved formulation for industrial use.

2.4 Grid refinement study

Three different grid distributions 50×50×500 (500 in the streamwise direction and 50×50 in the cross-stream directions), 65×40×1 000, 80×60×1 000 are tested for grid refinement study. The total numbers of grid cells are 1 148 383, 2 098 680 and 3 937 320 for the three investigated grids, and the numbers of nodes to resolve the boundary layer are 12, 15 and 20, respectively.

The calculated regional-averaged Nusselt number Nu on the leading surface for the three grid distributions at $Ro=0$ and $Ro=0.24$ is shown in Fig. 2, S is the actual length from the inlet of the duct. As seen the Nusselt number with coarse mesh 50×50×500 is overestimated in the second passage at $Ro=0.24$. The Nusselt number with finer mesh 65×40×1 000, as well as the grid 80×60×1 000, shows good agreement with the experiment data of Wagner, et al. [11], indicating that the grid 80×60×1 000 can provide a sufficient grid independency and accurate prediction. All of the following discussions are based on the grid 80×60×1 000.

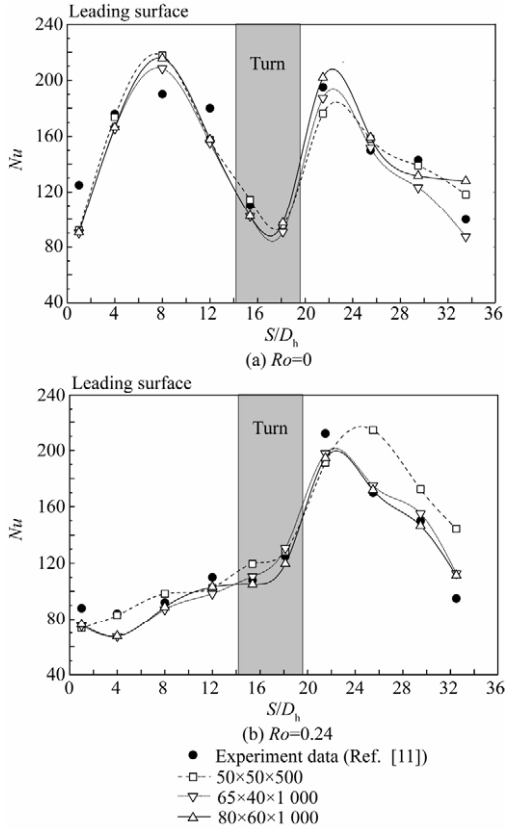

Fig. 2 Calculated regional-averaged Nusselt number on the leading surface for three grid distributions at Ro = 0, 0.24.

Moreover, to determine the sensitivity of model solutions to numerical discretization, the grid convergence index (GCI) method which is based on the generalized Richardson extrapolation [33-34] is employed here with the grid distributions 50×50×500, 65×40×1 000 and 80×60×1 000. The GCI indicates how much the solution would change with a further refinement of the grid. A small value of GCI indicates that the computation is within the asymptotic range. Table 1 presents the results of the grid convergency calculations using GCI method. The investigated parameters are the area-averaged Nusselt number on the leading surface under stationary ($Ro=0$) and rotating ($Ro=0.24$) conditions.

According to the GCI analysis shown in Table 1, several conclusions can be obtained. In Table 1, N is the total number of cells used for the computations, r is the grid refinement factor $r_{i,i+1}=\sqrt[3]{N_i/N_{i+1}}$. The approximate error E is calculated by $E_{i,i+1}=Nu_{i+1}-Nu_i$, and ε is the relative error $\varepsilon_{i,i+1}=|(Nu_{i+1}-Nu_i)/Nu_i|$. In the fine-grid convergence index,

$$\mathrm{GCI}_{\mathrm{fine}}^{i,i+1}=1.25\,\varepsilon_{i,i+1}\Big/(r_{i,i+1}^{p}-1) \tag{1}$$

where p is the order of numerical methods.

There is a reduction of GCI value for the grid refinements ($GCI_{21}<GCI_{32}$), indicating that the depend-

ency of numerical results on the cell size has been reduced. Also, a grid independent solution has been achieved. Further refinement of the grid will not give much change in the numerical results. In addition, the numerical uncertainties in the 80×60×1 000 grid solution adopted in the following simulations for the Nusselt number on the leading surface at Ro=0 and 0.24 are 10.13% and 5.07% , respectively.

Table 1 Results of grid convergency calculations

Ro	i	N_i	Nu_i	$r_{i,i+1}$	$E_{i,i+1}$	$\varepsilon_{i,i+1}$	$GCI_{fine}^{i,i+1}$/%
0	1	80×60×1 000	142	1.233	−5.81	0.040 9	10.13
	2	65×40×1 000	136.19	1.288	8.31	0.061 0	11.95
	3	50×50×500	144.5				
0.24	1	80×60×1 000	118.5	1.233	3.43	0.028 9	5.07
	2	65×40×1 000	121.93	1.288	4.57	0.037 4	5.11
	3	50×50×500	126.5				

3. Results and Discussion

In this section, the calculations for steam-cooled two-pass square channels with 45° ribs are performed. The calculated Nusselt number will be compared with the results of air-cooled channels. Then more numerical results will be analyzed in detail, including the velocity fields, temperature fields and Reynolds stresses.

The fluid properties in the Nusselt and Reynolds numbers are evaluated at the film temperature, i.e., T_f=(T_w+T_b)/2. The definition of the Nusselt number is

$$Nu = \frac{hD_h}{k} = \frac{q_w}{(T_w - T_b)} \cdot \frac{D_h}{k} \tag{2}$$

where q_w is the wall heat flux, h the heat transfer coefficient, T_b the local bulk temperature and k the thermal conductivity of coolant at the wall temperature.

3.1. Surface heat transfer for steam-cooled channels

Figures 3-4 show the comparison of averaged Nusselt number distributions between the steam-cooled and air-cooled channels at Re=25 000, Ro=0 and 0.24, respectively. Note that the calculated regional-averaged Nusselt number here is multiplied by 1.15 to compare with the data obtained by Wagner, et al. [11], except for the first and last points on both the leading and trailing surfaces, as well as the points at the bend region, where there are no ribs. The calculated Nusselt number is based on the true heat transfer area, while in Wagner, et al. [11], it is based on the projected area. The Nusselt number distributions for air-cooled and steam-cooled

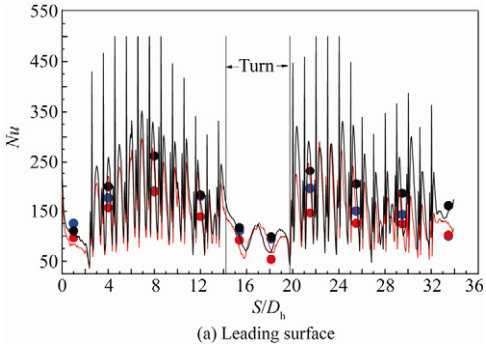

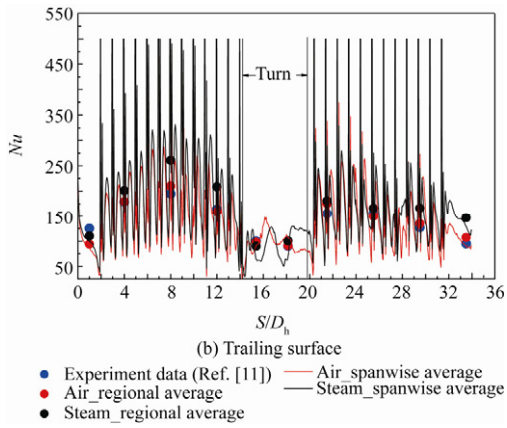

Fig. 3 Comparison for averaged Nusselt number between air-cooled and steam-cooled cases: Re=25 000, Ro =0.

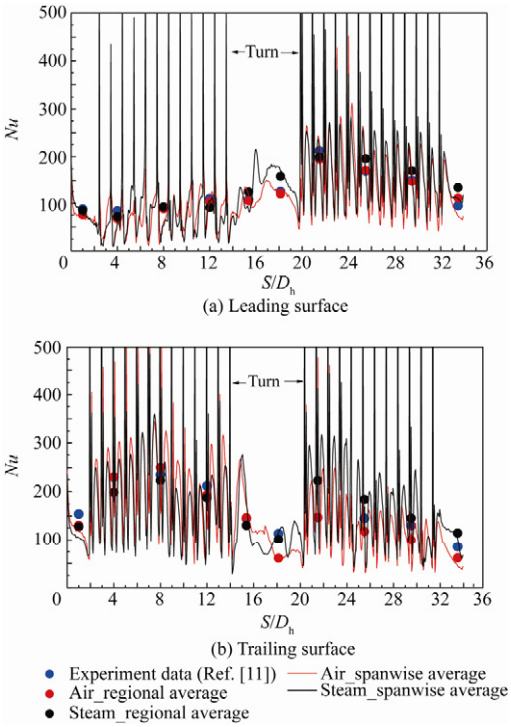

Fig. 4 Comparison for averaged Nusselt number between air-cooled and steam-cooled cases: Re=25 000, Ro=0.24.

channel show a similar tendency. However, the Nusselt number in the steam-cooled channels is higher, around 30% and 20% for the stationary and rotating cases, respectively. Since the superheated steam has high specific heat, density and thermal conductivity, it will show better cooling performance than air [35].

For the stationary case (see Fig. 3), the heat transfer distributions on the leading surface are similar to that on the trailing surface. The regional-averaged Nusselt number increases first and gets to the maximum at S/D_h=8, while it decreases to the minimum at the turning region due to the absence of ribs. When entering the second passage, the Nusselt number increases a lot suddenly and then decreases gradually in the streamwise direction. The spanwise-averaged Nusselt number distributions have periodic spikes. The higher spikes are caused by the flow impingement on the ribs, and the lower ones are caused by the flow reattachment between the ribs.

For the rotating case (see Fig. 4), in the first passage, the heat transfer on the leading surface is considerably weakened and the Nusselt number is much lower than that on the trailing surface, because the Coriolis force pushes the coolant towards the trailing surface. While in the second passage, the heat transfer on the leading surface is strengthened, and the Nusselt number on the leading surface is a little higher than that on the trailing surface, because the Coriolis force is reverse in the second passage, pushing the coolant towards the leading surface.

3.2. *Velocity and temperature fields for steamcooled channels*

The calculated three-dimensional velocity and temperature fields for both the non-rotating and the rotating 45° ribbed two-pass steam-cooled channels are presented in this section.

Figures 5-6 show the enlarged view of mean velocity vectors in the plane midway of the inner and outer surface for the stationary and rotating case, respectively. The location is between the 6th and 7th ribs on the leading surface in the first passage and the 6th and 7th rib in the second passage. Figure 5 indicates that the velocity near the leading surface is equal to that near the trailing surface in both the first and second passages in the stationary channels. In the first passage, there is obvious flow separation downstream of the ribs, but none in the second passage. Due to the 180° turning, the flow in the second passage is less sensitive to ribs.

While for the rotating case (see Fig. 6), in the first passage, the velocity vectors near the leading surface is much lower than that near the trailing surface. The flow separation occurs upstream and downstream of the ribs near the leading surface. The former is due to the Coriolis forces which push the coolant towards the trailing surface and the buoyancy force which tends to slow down the lighter fluid near the leading surface and accelerate the heavier fluid near the trailing surface. The latter is due to the rib turbulators. In the second passage, the mean velocity near the trailing surface and leading surface is almost equal again. This is because the Coriolis force acts in the opposite direction and pushes the cold fluids toward the leading surface. Thus the centrifugal buoyancy forces accelerate the lighter fluid near the trailing surface and, consequently, flatten the axial velocity profile.

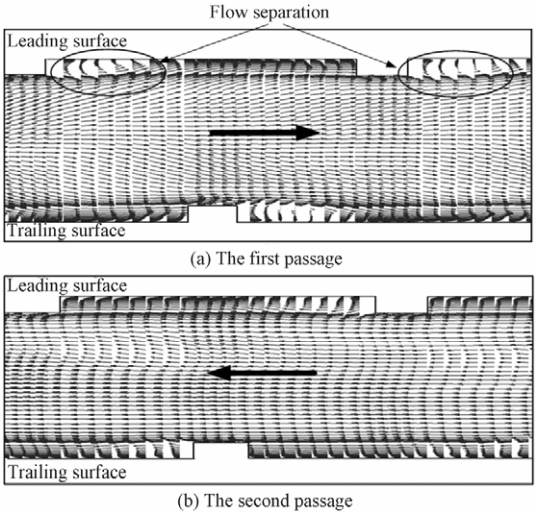

Fig. 5 Mean velocity ($0.1W_b$) fields for stationary steam-cooled channels.

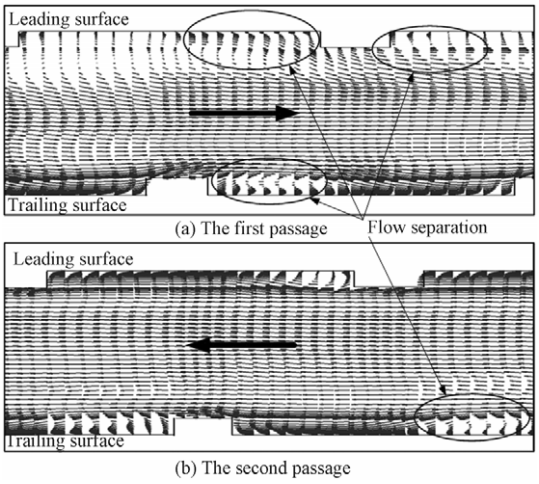

Fig. 6 Mean velocity ($0.1W_b$) fields for the rotating steam-cooled channels.

Figure 7 shows the cross-stream velocity vectors and the temperature contour at selected planes. As is shown in Fig. 1, Section *A* is $0.1D_h$ before the first rib on the trailing surface. Section *B* is on the top of the first rib and Section *C* is on the top of the second rib on the trailing surface. Section *D* is on the midway between the last rib on the trailing surface and the 12th rib on the leading surface. Section *E* is in the center of the bend. Section *F* is on the top of the first rib on the leading surface and Section *G* is between the last rib on

the trailing surface and the last rib on the leading surface in the second passage.

For the stationary case (see Fig. 7), it can be seen that in Section *A* (see Fig. 7 Section *A*), four small secondary corner vortices are produced by the anisotropy of the turbulent Reynolds stresses. As the coolant approaches the first rib (see Fig. 7 Section *B*), a narrow and long rib-induced vortex is generated near the top of the rib, pushing the coolant from the inner surface towards the outer surface. After passing through a pair of rib turbulators, two symmetric counter-rotating vortices occur near the outer surface, as is shown in Fig. 7 Section *C*. This secondary flow moves towards the outer surface and then returns back to the inner surface along the centerline, which leads to steep temperature gradient and high heat transfer coefficients on the ribbed surface and outer surface. In Fig. 7 Section *D*, these two symmetric counter-rotating vortices are full in size and occupy nearly half of the inclined cross-stream plane. In the bend (see Fig. 7 Section *E*), there are four big vortices. The vortices near the inner surface are induced by the ribs, and the two vortices near the outer surface are curvature induced secondary flow. After the bend, as the fluid enters the second passage, the curvature induced secondary flow overcomes the rib induced secondary flow. Consequently, vortices near the inner surface disappear, taken placed by two counter-rotating vortices which push the coolant from the inner surface to the outer surface. Meanwhile, there is a small rib induced vortex near the leading surface (see Fig. 7 Section *F*). As the coolant approaches the end of the second passage, the secondary flow moves along the top of the ribs towards the inner surface, and returns back to the outer surface along the centerline due to the ribs, as is shown in Fig. 7 Section *G*.

For the rotating case (Ro=0.24), the strong rotational Coriolis and buoyancy force greatly disturb the rib-induced secondary flow pattern in the stationary case. In Fig. 8 Section *A*, two narrow and long vortices near the inner and outer surfaces are caused by the Coriolis forces which push the coolant towards the trailing surface. When the coolant approaches the first rib (see Fig. 8 section *B*), another vortex induced by rib shows up on the rib tip. After the fluid moves through a pair of ribs along the passage (see Fig. 8 Section *C*), the vortex induced by the rib on the trailing surface becomes much larger than that near the leading surface, rather than two symmetric counter-rotating vortices shown in the stationary case (see Fig. 7 Section *C*). This is because the Coriolis force strengthens the secondary flow near the trailing surface and destroys the rib-induced flow near the leading surface. In the bend, the vortex induced by the ribs on the leading surface is totally occupied by the curvature induced vortex, while near the trailing surface, the vortex induced by ribs on the trailing surface is even bigger than the curvature induced vortex (see Fig. 8 Section *E*). This indicates that the secondary flow induced by Coriolis forces and ribs is much stronger than the secondary flow induced by turning centrifugal force.

After the bend, in Fig. 8 Section *F*, the curvature induced vortex has grown bigger than the rib induced vortex near the trailing surface. In Fig. 8 Section *G*, the

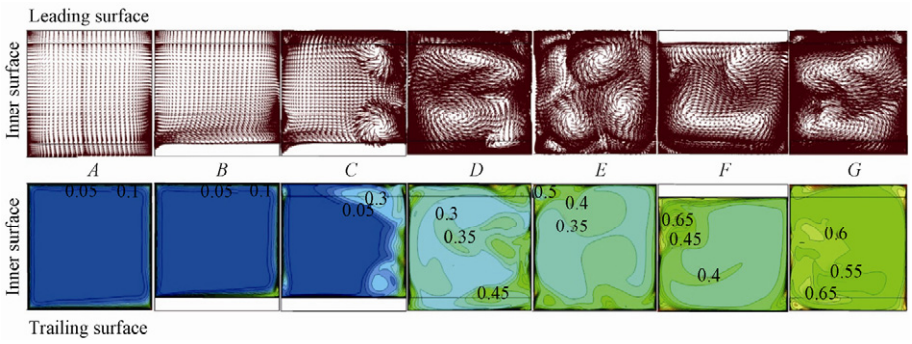

Fig. 7 Cross-stream velocity vector and dimensionless temperature contour for stationary channels.

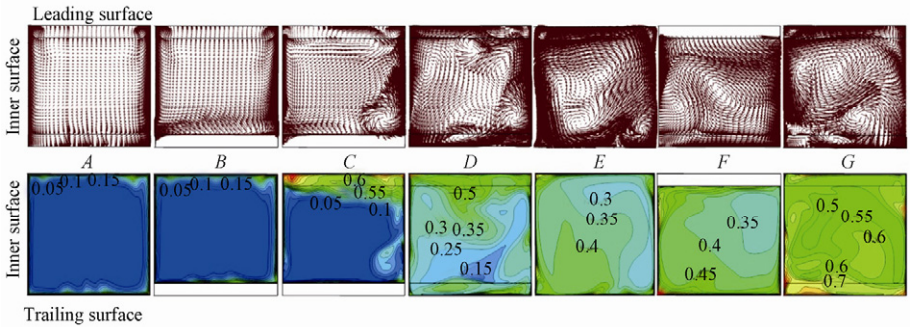

Fig. 8 Cross-stream velocity vector and dimensionless temperature contour for rotating channels.

vortex induced by the ribs on the leading surface is much larger than that near the trailing surface. This is because the Coriolis force acts on the reverse direction in the second passage.

3.3. Reynolds stresses

The rotational Coriolis force has an interesting characteristic that it is unable to affect the energy of a flow directly, because it is always perpendicular to the velocity. However it produces great anisotropic turbulence including both the Reynolds stresses and turbulent heat transfer. In this section the effects of anisotropic turbulence on detailed flow and heat transfer characteristics in steam-cooled channels will be discussed. The turbulent intensity is $\sqrt{uu}/W_b$, $\sqrt{vv}/W_b$ and $\sqrt{ww}/W_b$, where u, v, w are the turbulence velocity in three directions.The Reynolds stresses are presented at three selected planes: Sections D, E and F, which are shown in Fig. 1. For the stationary case, at Section D in the first passage (see Fig.9 (a)), the turbulent intensity is higher near the middle of the inner surface and at the corners near the trailing surface, where the velocity gradient changes sharply. This is because the eddy viscosity hypothesis assumes the Reynolds stresses to be proportional to the mean velocity gradients.

A rather high degree of anisotropy ($3.887\ 0 \le \overline{uu}/\overline{ww}$ or $\overline{vv}/\overline{ww} \le 2.387\ 0$) is observed near the middle of the inner surface and at the corner of leading and outer surfaces. Because the secondary flow pattern here is that the fluid moves towards the outer surface along the ribs and then returns to the inner surface along the centerline.

In the bend, the secondary flow is affected by the pressure-driven cross-stream flow in the turning and the turbulent intensity has been strengthened. The anisotropy is very high near the middle of each surface ($3.307\ 0 \le \overline{vv}/\overline{ww}$ or $\overline{uu}/\overline{ww} \le 2.463\ 8$), as well as the corners near the inner surface ($2.463\ 0 \le \overline{uu}/\overline{ww}$ or $\overline{vv}/\overline{ww} \le 2.970\ 0$). After the bend (see Fig. 9 (c)), the level of turbulent intensity is as high as 18% near the outer surface due to the bend effect while it has a tendency to move towards the inner surface, because of the pressure-driven cross-stream flow.

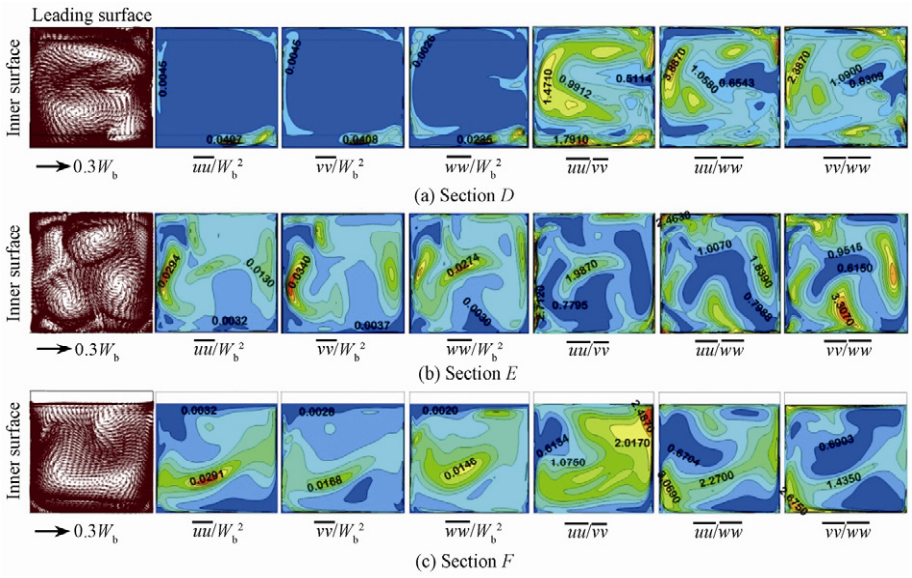

Fig. 9 Reynolds stresses for stationary channels.

For the rotating case, in the first passage (see Fig. 10), the turbulent intensity ($\sqrt{uu}/W_b$, $\sqrt{uu}/W_b$ and $\sqrt{ww}/W_b$) is enhanced greatly due to the Coriolis and rotating buoyancy forces compared with the stationary case. It can be observed that the highest level of turbulent intensity occurs around the rib on the leading surface, probably as high as 20%-26%, because of the flow separation on the top of the ribs on the leading surface (see Fig. 6(a)), indicating that the flow separation can lead to higher turbulent intensity. In the bend the higher level of turbulence intensity seems to move towards the trailing surface and the turbulence intensity in the core region increases compared with the stationary case (see Fig. 9(b)). The anisotropy at the corners is much higher ($2.368\ 0 \le \overline{uu}/\overline{ww}$ or $\overline{vv}/\overline{ww} \le 3.528\ 0$), so corner vortices form at the corners.

In the second passage, the turbulence intensity is higher near the inner surface where the vortices meet, as much as 24%. A rather high degree of anisotropy ($3.887\ 0 \le \overline{uu}/\overline{ww}$ or $\overline{vv}/\overline{ww} \le 2.387\ 0$) is observed near the middle of the inner surface and at the corner of leading and outer surfaces, since the secondary flow pattern here is that the fluid moves towards the outer surface along the ribs and then returns to the inner sur face along the centerline.

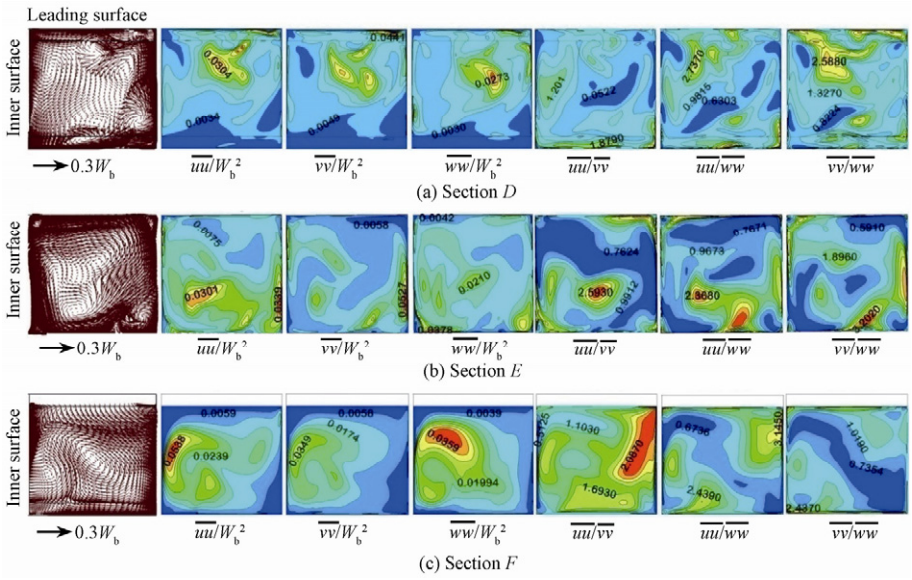

Fig. 10 Reynolds stresses for rotating channels.

4. Conclusions

1) The calculated Nusselt number for steam-cooled and air-cooled two-pass square channels shows a similar tendency in both the stationary and rotating cases, and the Nusselt number is much higher in the steam-cooled channels. The superheated steam shows better cooling performance than air.

2) For the steam-cooled channels considered here, the Coriolis and buoyancy forces weaken the heat transfer on the leading surface in the first passage while strengthen it in the second passage. The combined effect of rib turbulators, 180° sharp turning and rotation leads to very complex flow patterns in the channels.

3) The Coriolis and rotating buoyancy forces produce strong Reynolds stresses and the anisotropic turbulence, which significantly affect the heat transfer distributions on the surfaces.

References

[1] Goldstein R J. Film cooling. Advances in Heat Transfer 1971; 7(1): 321-379.
[2] Moffat R J. Turbine blade cooling. Symposium on Heat Transfer in Rotating Machinery. 1985.
[3] Metzger D E, Berry R A, Bromson J P. Developing heat transfer in rectangular ducts with staggered arrays of short pin fins. Journal of Heat Transfer 1982; 104(4): 700-706.
[4] Metzger D E, Haley S W. Heat transfer experiments and flow visualization for arrays of shortpin fins. ASME Paper, 1982-GT-138, 1982.
[5] Metzger D E, Fan S C, Haley S W. Effects of pin shape and array orientation on heat transfer and pressure loss in pin fin arrays. Journal of Engineering for Gas Turbines and Power 1984; 106(1): 252-257.
[6] Han J C. Heat transfer and friction in channels with two opposite rib-roughened walls. Journal of Heat Transfer 1984; 106(4): 774-781.
[7] Han J C, Park J S. Developing heat transfer in rectangular channels with rib turbulators. International Journal of Heat and Mass Transfer 1988; 31(1): 183-195.
[8] Chupp R E, Helms H E, McFadden P W, et al. Evaluation of internal heat transfer coefficients for impingement cooled turbine airfoils. Journal of Aircraft 1968; 6: 203-208.
[9] Metzger D E, Bunker R S. Local heat transfer in internally cooled turbine airfoil leading edge regions: Part II—impingement cooling with film coolant extraction. Journal of Turbomachinery 1990; 112(3): 459-466.
[10] Yanovski L S. Physical basis of transpiration cooling for engines of flying apparatus. Moscow: MAI Press, 1996.
[11] Wagner J H, Johnson B V, Han J C. Heat transfer in rotating passages with smooth walls and radial outward flow. Journal of Turbomachinery 1991; 113(1): 42-51.
[12] Wagner J H, Johnson B V, Kopper F C. Heat transfer in rotating serpentine passages with smooth walls. Journal of Turbomachinery 1991; 113(3): 321-330.
[13] Wagner J H, Johnson B V, Graziani R A, et al. Heat transfer in rotating serpentine passages with trips normal to the flow. Journal of Turbomachinery 1992; 114(4): 847-857.
[14] Johnson B V, Wagner J H, Steuber G D, et al. Heat transfer in rotating serpentine passages with trips skewed to the flow. Journal of Turbomachinery 1994; 116(1): 113-123.
[15] Han J C, Zhang Y M. Effect of uneven wall temperature on local heat transfer in a rotating square channel with smooth walls and radial outward flow. Journal of Heat Transfer 1992; 114(4): 850-858.
[16] Azad G S, Uddin M J, Han J C. Heat transfer in a two-pass rectangular rotating channel with 45-deg angled rib turbulators. Journal of Turbomachinery 2002; 124(2): 251-259.
[17] Wright L M, Fu W L, Han J C. Thermal performance of angled V-shape, and W-shaped rib turbulators in rotating rectangular cooling channels (AR=4:1). Journal of Turbomachinery 2004; 126(2): 604-614.
[18] Liu Y H, Huh M, Han J C. Heat transfer in a two-pass rectangular channel (AR=1:4) under high rotation

numbers. Journal of Heat Transfer 2008; 130(8): 081701-081709.
[19] Fu W L, Wright L M, Han J C. Rotational buoyancy effects on heat transfer in five different aspect-ratio rectangular channels with smooth walls and 45 degree ribbed walls. Journal of Heat Transfer 2006; 128(11): 1130-1141.
[20] Wright L M, Fu W L, Han J C. Influence of entrance geometry on heat transfer in rotating rectangular cooling channels (AR=4:1) with angled ribs. Journal of Heat Transfer 2005; 127(4): 378-387.
[21] Dutta S, Andrews M J, Han J C. Prediction of turbulent heat transfer in rotating smooth square ducts. International Journal of Heat and Mass Transfer 1996; 39(12): 2505-2514.
[22] Stephens M A, Shih T I P, Civinskas K C. Computations of flow and heat transfer in a rotating U-shaped square duct with smooth walls. AIAA-1996-3161, 1996.
[23] Chen H C, Jang Y J, Han J C. Computation of heat transfer in rotating two-pass square channels by a second-moment closure model. International Journal of Heat and Mass Transfer 2000; 43(9): 1603-1616.
[24] Chen H C, Jang Y J, Han J C. Near-wall second- moment closure for rotating multi-pass cooling channels. Journal of Thermophysics and Heat Transfer 2000; 14(2): 201-209.
[25] AI-Qahtani, M S, Jang Y J, Chen H C, et al. Prediction of flow and heat transfer in rotating two-pass rectangular channels with 45-deg rib turbulators. Journal of Turbomachinery 2002; 124(2): 242-250.
[26] MacDonell B, McDonough P, Boral K, et al. Steam cooling hits the mark. Power Engineering International 2006; 14(2): 29-31.
[27] Varley J. GT steam cooling--who needs it? (Gas turbines). Modern Power Systems. 2006.
[28] Beedie M, Writer F. GE's H-series breaks 60% fuel efficiency barrier. <http://www.power-technology.com>. 2007.
[29] Corman J C H. Gas turbine combined cycle power generation system for the future. Proceedings of Yokohama International Gas Turbine Congress. 1995.
[30] Fukue I. A new generation of advanced gas turbine. Proceedings of Yokohama International Gas Turbine Congress. 1995.
[31] "ANSYS CFX Introduction", ANSYS CFX Release 11.0. <http://www.ansys.com>. 2006.
[32] Wagner W, Cooper J R, Dittman A, et al. The IAPWS industrial formulation 1997 for the thermodynamic properties of water and steam. Journal of Engineering for Gas Turbines and Power 2000; 122(1): 150-184.
[33] Scheuler M, Neumann S O, Weigand B. Numerical investigations of pressure loss and heat transfer in a 180° bend of a ribbed two-pass internal cooling channel with engine-similar cross-sections. Proceedings Institution of Mechanical Engineers. Part A: Journal of Power and Energy 2010; 224(3): 349-361.
[34] Celik I B, P J, Ghia U, Roache P J, et al. Procedure for estimation and reporting of uncertainty due to discretization in CFD applications. Journal of Fluids Engineering-Transactions of the ASME 2008; 130(7): 078001-078004.
[35] Shui L Q, Gao J M, Xu L. Numerical investigation of heat transfer and flow characteristics in a steam-cooled square ribbed duct. ASME Paper, 2010-GT-22407, 2010.

Biographies:

WANG Wei received B.S. degree from Xi'an Jiaotong University in 2008, and now she is working on her Ph.D. degree there. Her main research interest is turbine blade cooling technology.
E-mail: vivian.533@stu.xjtu.edu.cn

XU Liang received B.S. degree from Harbin Engineering University in 2003 and Ph.D. degree from Harbin Institute of Technology in 2009. Now he is working in Xi'an Jiaotong University as a lecturer. His main research interest is turbine blade cooling technology.
E-mail: xuliang@mail.xjtu.edu.cn